Journal of
Instrumentation

Development and performance assessment of the BGO calorimeter module for the FOOT experiment

To cite this article: N. Bartosik *et al* 2025 *JINST* **20** P03021

Published by IOP Publishing for Sissa Medialab

Received: *September 26, 2024*
Accepted: *January 5, 2025*
Published: *March 19, 2025*

Development and performance assessment of the BGO calorimeter module for the FOOT experiment

The FOOT collaboration

E-mail: piergiorgio.cerello@to.infn.it

Abstract: FOOT (FragmentatiOn Of Target) is a nuclear physics experiment currently under construction that will measure differential cross sections for the production of secondary fragments induced by the interactions of proton and ion beams, up to 400 MeV/u, with human tissues. By extending the energy range to about 800 MeV/u, FOOT will also provide data useful to radio-protection in space, as understanding fragmentation processes that take place in spacecraft shieldings is crucial to their optimisation. The FOOT collaboration is building a detector designed for the identification of heavy fragments in an inverse-kinematics configuration, through the measurement of their momentum, energy and time-of-flight with very high resolution.

The kinetic energy of the fragments will be measured with a BGO calorimeter that must cover a dynamic range from tens of MeVs to about 10 GeV and achieve an energy resolution smaller than 2%. In this work we report about the R&D steps that led to the design choices and we assess the performance of the calorimeter prototype. Several beam tests have been performed at CNAO (Pavia, Italy) to choose the best photodetector, crystal wrapping, front-end electronics and readout, in order to achieve the required performance in terms of linearity and energy resolution.

Measurements on the first assembled module, made of 3×3 BGO crystals with truncated pyramid shape, coupled to SiPM photodetectors, show that, up to at least 5 GeV of deposited energy, there is no saturation effect related to optical photon pileup in the SiPM microcells and the energy resolution ranges from about 2% standard deviation for 70 MeV protons to less than 0.5% for 400 MeV/u carbon ions. This level of performance has been achieved on data collected within a temperature range of about 10°C.

Deviations from linearity were studied by calibrating the crystals with monochromatic beams impinging both on the front face and at different positions along its side. Correction methods to compensate for the signal loss as a function of the range (i.e., the energy) and for temperature fluctuations, were developed and validated on experimental data.

Presently, the full calorimeter construction (320 BGO crystals) is complete.

Keywords: Calorimeter methods; Calorimeters

https://doi.org/10.1088/1748-0221/20/03/P03021

Contents

1 Introduction 1

2 Materials and methods 2
  2.1 The FOOT calorimeter 2
  2.2 Measurements 3
  2.3 BGO Crystals 4
  2.4 Photodetectors 4
  2.5 Readout 4
  2.6 Temperature correction 5
  2.7 Depth-dependent response 6
  2.8 Mechanics 6

3 Results 7
  3.1 SiPM tile selection 7
  3.2 Crystal coating 8
  3.3 Temperature correction 9
  3.4 Calibration and range correction 10
  3.5 Linearity 11
  3.6 Energy resolution 11
  3.7 Shape analysis 13

4 Discussion 14

The FOOT collaboration 17

1 Introduction

In the last decade a continuous increase in the number of cancer patients treated with Charged Particle Therapy (CPT) [1] has been registered. The effectiveness of CPT in the treatment of deep-seated solid tumours [2] derives from the depth-dose profile of charged particles, characterised by a low dose release in the entrance channel, followed by a narrow region, the Bragg Peak (BP), where the maximum of the dose is deposited. However, a not negligible fraction of the beam particles ($\sim 40\%$) undergoes nuclear processes and can cause beam (in the case of ions) and target (i.e., tissue) fragmentation, that is the cause of about 10% of the biological effect induced in the entrance channel [3]. When the beam crosses the patient tissues on its way to the target volume, nuclear interactions can occur: target fragmentation generates heavy recoils with short range (e.g., 10–100 μm), very high Linear Energy Transfer and therefore high Relative Biological Effectiveness. In case of ion beams, their fragments also cause an energy deposition tail beyond the BP region. In order to optimize the treatment plan, a precise knowledge of the beam-target cross section for the production of different types of fragments is therefore fundamental.

The fragmentation of light ions on light targets is also relevant for radio-protection in space, in view of long duration manned missions, such as for example the journey to Mars [4, 5]. Solar Particle Events (SPEs) and Galactic Cosmic Rays (GCR) are the main sources of energetic particles in space. SPEs are mainly composed of protons, with an energy spectrum that peaks just before the *GeV* region, and could inflict a lethal dose to the astronauts. Since the radiation field reaching the astronauts is modified by the interaction with the walls of the spacecraft, the design optimisation of the spacecraft shielding requires a detailed knowledge of fragmentation processes.

FragmentatiOn Of Target (FOOT) is a nuclear physics experiment, whose construction is close to completion, that will measure fragmentation cross sections for light ion beams up to 800 MeV/u on proton/carbon rich targets. It will operate in inverse kinematics, so that the increase in the fragment range resulting from the kinematic boost will allow their escape from the target volume and make their detection possible. In order to calculate fragmentation cross sections for specific isotopes with resolutions better than 5%, fragments must be identified through the measurement of their momentum, energy and time of flight with resolutions of 5%, 2%, and 100 ps, respectively.

To achieve these goals, the detector is composed of: a plastic scintillator, called Start Counter, to determine the time of arrival of the beam; a drift chamber, called Beam Monitor, to determine the position of the beam; a magnetic spectrometer, to determine the fragment momenta; the TOF Wall, consisting of two layers of plastic scintillation bars, for time-of-flight measurement; the calorimeter, described in the following. Further details are provided in [6].

Simulations based on the FLUKA code [7, 8] show that heavy fragments ($Z \geq 3$) are forward-peaked within a polar angle of about 6° and with a kinetic energy per nucleon peaked around the corresponding value of the primary beam, while light fragments show a wider angular and kinetic energy distribution [9]. The design of FOOT layout includes a BGO crystal calorimeter that measures the kinetic energy of fragments and contributes to identifying their mass.

In this work we report about the R&D process that led to the design of the calorimeter. The choices related to the best photodetector and its configuration, crystal wrapping, front-end electronics and readout are discussed in detail, as well as the calorimeter performance, in terms of linearity and energy resolution, and the correction methods developed to optimise it. The shape of BGO signals was also studied as a function of the beam particle, energy and beam position along the side of the crystal, in order to assess the feasibility of using the signal rising time as one of the inputs for the fragment Z measurement.

2 Materials and methods

2.1 The FOOT calorimeter

The calorimeter (figure 1), positioned behind the thin plastic scintillator layer as the last detector in the FOOT layout [6], stops the fragments and, by measuring their kinetic energy, completes the set of observables required to identify them (Time of Flight, momentum, kinetic energy). In order to meet the goal of providing fragmentation cross sections with at least 5% accuracy, the calorimeter must achieve an energy resolution, defined as the ratio between the sigma and the mean of the energy distrbution, below 2% [6]. BGO crystals were already available from a previous experiment, but the choice of their coating and of the photodetector, the design of the front-end board, the DAQ system and the mechanical structure were the subject of a dedicated R&D process. The calorimeter

2025 JINST 20 P03021

layout was designed to cover the area that will be spanned by high energy fragments originating from interactions in the target, as evaluated from FLUKA-based Monte Carlo simulations [6]: at about 1.2 m from the target, the angular coverage is about 11°.

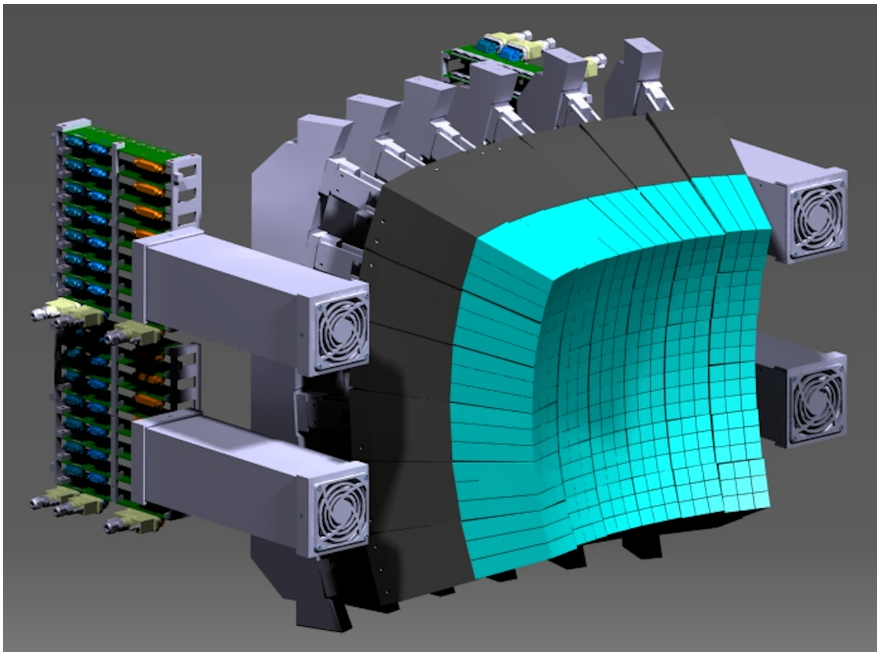

Figure 1. The calorimeter layout: BGO crystals (light blue) will be mounted in 3D-printed 3×3 modules, kept in the nominal position from the back by mechanical holders. On the sides, 4 fans will provide the air flow required to keep the temperature of the whole system within an acceptable range, and 32 boards will distribute the high and low voltage supply to the front-end boards and will transmit the temperature values for each crystal.

2.2 Measurements

All the experimental measurements required to optimize the calorimeter configuration took place at the CNAO facility (Centro Nazionale di Adroterapia Oncologica, Pavia, Italy, https://fondazionecnao.it/). Although the CNAO beam monitor is optimised for clinical beam intensities (up to 5×10^7 Hz and 5×10^9 Hz for carbon ions and protons, respectively), the synchrotron was tuned for the delivery of low intensity ($\sim 10^4$ Hz) beams at a set of predefined energies (70, 120, 170 and 227 MeV for protons, 115, 190, 260, 330 and 399 MeV/u for carbon ions), so as to cover the whole accessible energy spectrum and allow the study of the calorimeter response in terms of linearity and energy resolution. In the following, we will refer to an energy scan as a sequence of acquisitions that includes the beam delivery at each of the 9 above-listed energy values.

Table 1. Parameters of the 3 SiPM tiles tested as possible FOOT photodetectors.

Sample	Type	Number of channels	Cell Size (mm^2)	Microcell pitch (µm)
NUV-HD30	NUV	16	6×6	30
RGB-HD20	RGB	30	4×4	20
RGB-HD15	RGB	30	4×4	15

2025 JINST 20 P03021

2.3 BGO Crystals

The calorimeter, whose layout is shown in figure 1, will be composed of 320 BGO crystals reused from a previous experiment, with a truncated pyramid shape, a front side of $20 \times 20\,\mathrm{mm}^2$, a rear side varying from $27 \times 27\,\mathrm{mm}^2$ to $29 \times 29\,\mathrm{mm}^2$ and a length of 240 mm, that will be positioned with a square arrangement with a side of about 40 cm.

The BGO high density ($\rho = 7.13\,\mathrm{g/cm}^3$) guarantees a high stopping power: in most of the energy range that FOOT will explore, the charged fragments are fully contained in their volume, except for the fraction that, through nuclear interactions, generates neutrons that can escape the detector. Above $\sim$ 280 MeV/u, $\pi^{\pm}$ production is also possible, causing an energy leak from the calorimeter and a corresponding performance degradation (i.e., a fraction of the incoming particles does not release completely its energy in the BGO).

2.4 Photodetectors

In principle, both Photo-Multiplier Tubes (PMTs) and Silicon Photo-Multipliers (SiPMs) are suitable as photodetectors to be coupled to the BGO crystals. SiPMs arrays, however, provide two crucial advantages: a compact design and a relatively low (30–40 V) voltage power supply. However, they should operate in a range where the effect of optical photons pileup in a SiPM microcell is negligible, so as to minimize deviations from linearity in the response over the full energy range covered by the fragments to be detected: from tens of MeV for low energy protons to about 10 GeV, corresponding to C or O beam particles up to 800 MeV/u. To ensure linearity, the choice of the microcell pitch and reset time is crucial. Preliminary estimates suggested that, taking into account the slow BGO response (300 ns decay time constant) and its light yield, a linear response should be achieved for a microcell pitch up to 20 µm, as long as the microcell reset time is smaller than 10 ns. In order to verify the SiPM response linearity up to 400 MeV/u carbon beams (4.8 GeV), three different prototypes (see table 1) provided by Fondazione Bruno Kessler (FBK) were tested with monochromatic carbon beams at the 5 above-listed energies.

The tile (figure 2) is rectangular ($23 \times 22\,\mathrm{mm}^2$), with 25 cells of $4 \times 4\,\mathrm{mm}^2$ size, and features a $400\,\mathrm{mm}^2$ active area, corresponding to about 48–55% of the crystal back area. It was glued to the crystal back face by means of the Dowsil 3145 adhesive. Changes in temperature cause variations in the photodetector breakdown voltage, hence affecting system response, therefore the temperature must be monitored throughout the data collection. The SiPM tile features an NTC thermistor for this purpose.

2.5 Readout

The front-end board must provide the power supply to the SiPM tiles (figure 2(a)), process the output signals and measure the SiPM temperature through the NTC. It was designed to match the tile size and maximise the compactness. Figure 2(b) and 2(c) show the two sides of the front-end board, which is then mounted on the SiPM tile as shown in figure 2(d). The signal from 5 of the 25 SiPM cells is summed and pre-amplified by a commercial LT1396 operational amplifier. The output of the 5 groups is then summed, using the same device, into a single output that is sampled by a high-frequency digitizer module. The digitized waveform is stored for each triggered event, and maximum amplitude and time information are extracted offline.

Three different digitisers were tested: *CAEN V1740* (62.5 MS/s sampling frequency, 10 Vpp output range), *CAEN V1742* (up to 5 GS/s sampling frequency, 1 Vpp output range) and *WaveDAQ*[10] (up to 5 GS/s sampling frequency, 1 Vpp output range, attenuator up to 0.5). All provide a comparable

2025 JINST 20 P03021

performance in terms of energy resolution; however, as discussed in section 3, *WaveDAQ* allows a better measurement of the shape of the signal as well as its timing. In addition, *WaveDAQ* is also used as readout for the Start Counter and TOF Wall detectors, and it therefore simplifies the integration of the calorimeter signals in the trigger logic.

Examples of digitised signals for 399 MeV/u carbon ions are shown in figure 3. The shaping introduced by the AC decoupling in the *WaveDAQ* digitizer front-end causes a long signal undershoot, which, however, does not affect the maximum amplitude measurement. The signal is parametrized according to equation (2.1) [11]:

$$A(t) = A_{\mathrm{MAX}} \exp(k_s \ln^2((t - t_0)/t_r)) \tag{2.1}$$

and the fit yields the starting time (t_0), the rising time (t_r), that is the time at which the signal takes its maximum amplitude (A_{MAX}), and k_s, that embeds the parametrization of the signal shape.

As an example, the parameter values for a typical signal shape are shown in table 2.

Table 2. Parameters of a typical waveform acquired with the*CAEN V1740, CAEN V1742* and *WaveDAQ* digitizers.

	V1740	*V1742*	*WaveDAQ*
A (mV)	7.09e+02	5.51e+02	8.94e+02
t_0 (ns)	1.33e+02	1.28e+02	1.22e+02
t_r (ns)	5.35e+01	3.31e+01	3.85e+01
k_s (a.u.)	1.86e−01	1.91e−01	4.02e−01

The time integral is evaluated from the fit function, integrating from t_0 to $t_0 + t_{\mathrm{max}}$, with $t_{\mathrm{max}} = 800$ ns for the *CAEN V1740* and *CAEN V1742* digitizers, $t_{\mathrm{max}} = 200$ ns for *WaveDAQ*.

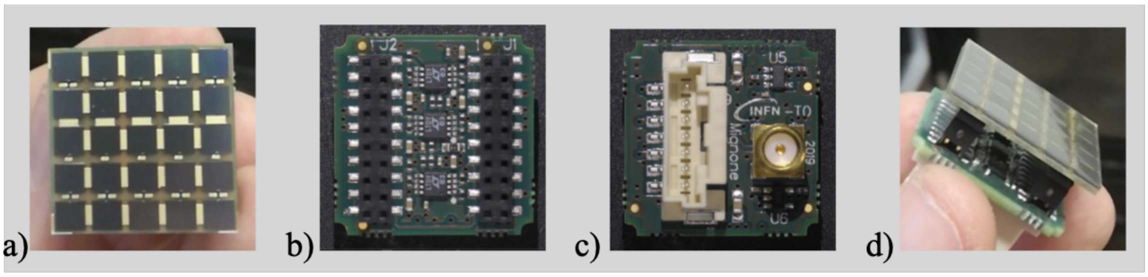

Figure 2. (a) The SiPM tile selected for the final calorimeter design: with a $23 \times 22\,\mathrm{mm}^2$ size, it features 25 cells of $4 \times 4\,\mathrm{mm}^2$ size and a $400\,\mathrm{mm}^2$ active area, corresponding to about 48–55% of the crystal backend. (b) Front-end board from the side that connects to the SiPM tile. (c) Front-end board from the side that connects to the power supply and DAQ system. (d) SiPM tile and Front-end board.

2.6 Temperature correction

Since FOOT will acquire data at different facilities (CNAO, GSI, etc.), likely at different temperatures, a study of the stability of the calorimeter response as a function of the temperature is crucial. The BGO light yield [12] and the SiPM gain are both sensitive to temperature and require either very stable operational conditions or a method for compensating temperature variations. Indeed, when monitoring the temperature variation during energy scans with the proton and carbon beams at CNAO for a single crystal irradiation, a slow and steady increase with time was observed. In order to assess the relevance of the temperature dependence, the energy scan was repeated 4 times: one at room temperature, and the others with a heat gun aimed at the SiPM tile at different distances. The maximum observed variation was about 10°C. From the measurement of the amplitude and temperature, it is possible, by interpolating the slope values at T_1 and T_2, to compute the actual slope (m) to be used for correcting amplitude measurements (T, A), which is obtained as [13]:

$$|m| = A/(T_{\mathrm{meas}} - T_{\mathrm{ref}}) \tag{2.2}$$

2.7 Depth-dependent response

In order to fully characterise the BGO/detector response, as well as define and optimize the energy calibration protocol, carbon ion beams of 115 and 260 MeV/u and proton beams of 70 and 170 MeV were aimed at the lateral side of 2 BGO crystals, at different positions, as shown in figure 4. The beam was delivered starting from $x = 15$ mm from the front side ($x = 0$) of the crystal, with a 30 mm step, up to $x = 225$ mm, the closest position to the SiPM tile (which is located at $x = d = 240$ mm). The energy of proton and carbon ion beams was selected in such a way that the Bragg Peak was either in the first (for 70 MeV protons and 115 MeV/u carbon ions) or in the second crystal (for 170 MeV protons and 260 MeV/u carbon ions), as shown in figure 4(b). The Bragg Peak expected positions, according to simulations performed with the FLUKA Monte Carlo, are summarized in table 3.

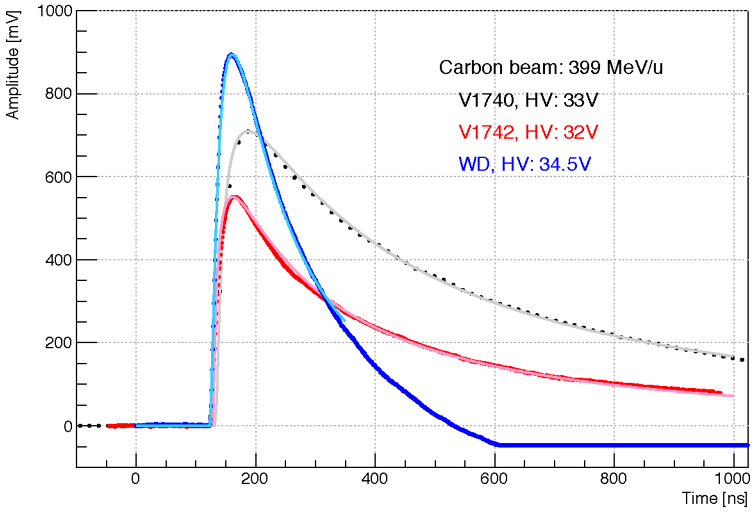

Figure 3. Examples of SiPM signals from 399 MeV/u carbon ions sampled by the *CAEN V1740* (black), *CAEN V1742* (red) and *WaveDAQ* (blue) digitisers at 62.5 MS/s, 1 GS/s and 1 GS/s, respectively. The shaping introduced by the AC decoupling in the *WaveDAQ* digitizer front-end causes a long signal undershoot, which, however, doesn't affect the maximum amplitude measurement.

2.8 Mechanics

The main requirement of the calorimeter mechanical structure is that once fragments coming from the target reach the calorimeter, they should not cross anything but air and the BGO crystals. Since the range in BGO of the most energetic fragments will not exceed 7 cm, the 3D-printed modules support structure was designed to hold the crystals in position from the back in such a way that the first 12 cm are free of additional material; the whole structure will be mounted according to the drawing shown in figure 1.

Table 3. Expected Bragg Peak positions for proton and carbon ions for the energies selected in the measurements. Values were obtained with a Fluka Monte Carlo simulation.

Particle	Energy (*MeV/u*)	Bragg Peak depth in BGO (*mm*)
proton (*p70*)	70	8.2
proton (*p170*)	170	45.1
Carbon (*C115*)	115	6.7
Carbon (*C260*)	260	30.3

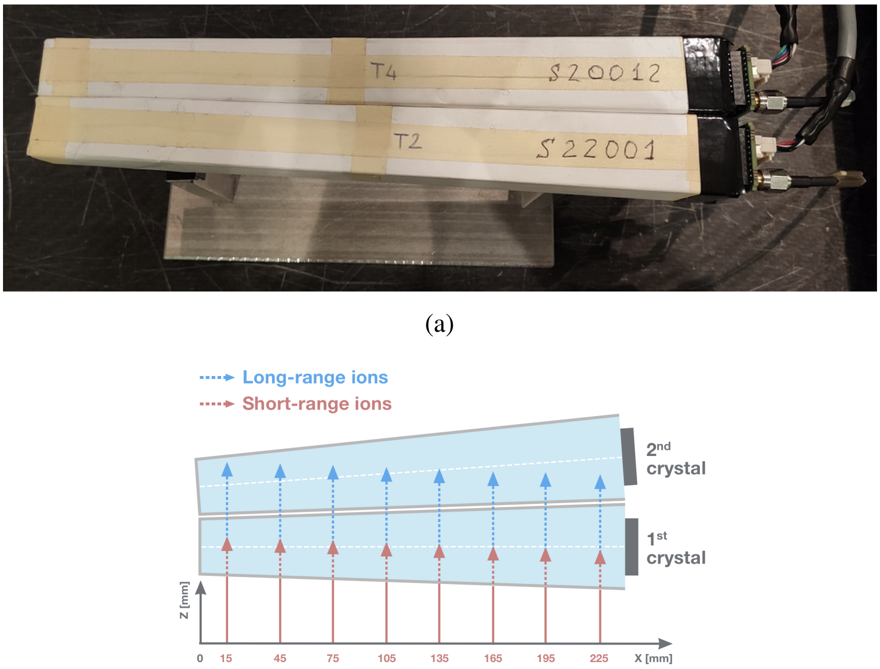

(a)

(b)

Figure 4. Top view of the two BGO crystals used for the data acquisition (a). The beam was fired on the lateral side of the crystal at different positions, with 30 mm steps. The thickness of two crystals is sufficient to stop 70 MeV protons, 115 and 260 MeV/u carbon ions; for 170 MeV protons the range is shorter than the overall crystal thickness only for $x > 120$ mm.

3 Results

3.1 SiPM tile selection

The response from the 3 prototypes (NUV-HD30, RGB-HD20, RGB-HD15) is shown in figure 5. While the RGB-HD15 and RGB-HD20 prototypes, with 15 µm and 20 µm microcell pitch respectively, show a close-to-linear behaviour, a clear non-linearity, reflected in the linear fit χ^2 values, is observed for the NUV-HD30 tile, with 30 µm microcell pitch. Therefore, both the RGB-HD20 and the RGB-HD15 models would be suitable options. In order to extend as much as possible the dynamic range of the calorimeter, the RGB-HD15 tile was selected: its Photo Detection Efficiency (PDE) is maximum between 500 and 600 nm and increases with the OverVoltage (OV); accordingly, the gain linearly increases with the *OV* (figure 6).

2025 JINST 20 P03021

3.2 Crystal coating

The raw BGO response as a function of the beam energy, reported in figure 7 in terms of Maximum Amplitude, shows that crystals wrapped in Tyvek provide the highest light collection on the SiPM. Therefore, Tyvek was preferred to Mylar and Reflective White Painting as crystal coating. Moreover, Tyvek is also more resistant than Mylar and Paint, which would be easily scratched during the assembly and transportation procedures. Therefore, Tyvek was selected as crystal coating.

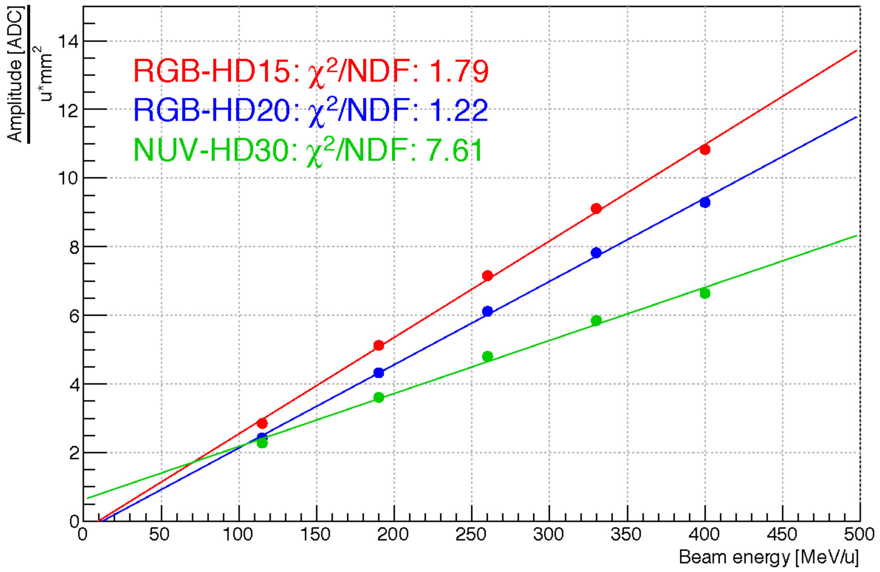

Figure 5. Average values of the response of the 3 SiPM tile prototypes as a function of the beam energy for carbon ion beams and the corresponding linear fits. The raw response for the NUV-HD30 tile with 30 µm microcell pitch (green) clearly shows a significant deviation from linearity at the highest carbon beam energies; the response for the RGB-HD15 and RGB-HD20 tiles, with 15 (red) and 20 (blue) µm microcell pitch, respectively, is close to linearity. The error bars are smaller than the marker size.

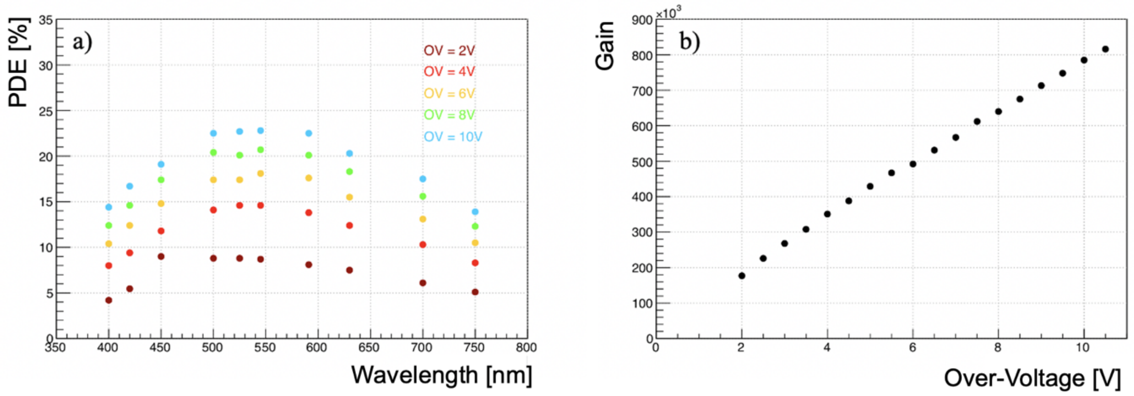

Figure 6. RGB-HD15 SiPM tile specifications, as provided by FBK: (a) Photo Detection Efficiency (PDE) as a function of the wavelength for different values of the OverVoltage (OV); (b) gain as a function of OV.

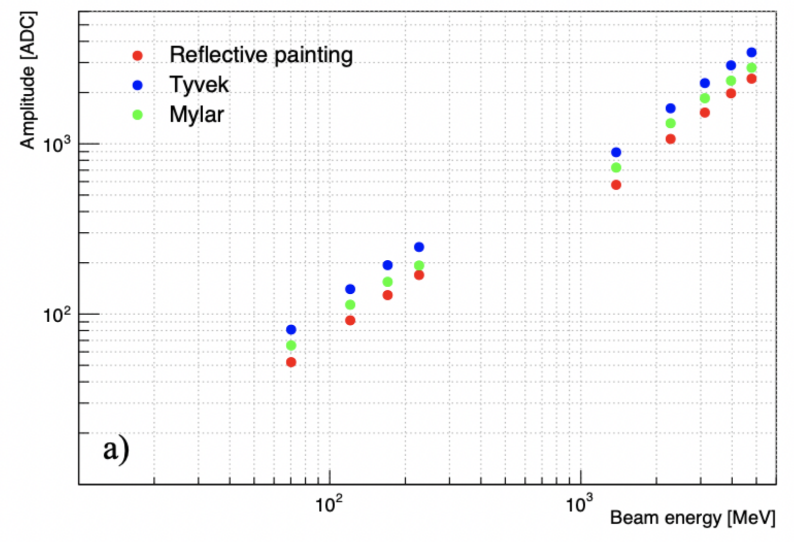

Figure 7. SiPM response as a function of the total beam energy: maximum amplitude for crystals wrapped with Reflective painting (red), Tyvek (blue) and Mylar (green). Error bars are smaller than the size of markers.

3.3 Temperature correction

Data collected at different temperatures on the same crystal, shown in figure 8(a), highlight a linear dependency of the SiPM response (scaled by the number of nucleons in the incoming beam) on the temperature, with an angular coefficient that slightly increases with the energy. Each set of points was fitted by a straight line, and the slope parameter of each fit has been evaluated and studied as a function of amplitude at the selected reference temperatures T_1 (25°C) and T_2 (33°C).

The observed signal variation rate, which combines the effects of a change in BGO light yield and in the SiPM gain (both decreasing), is about $-1.4\%/°\text{C}$, consistent with previous measurements [12, 14].

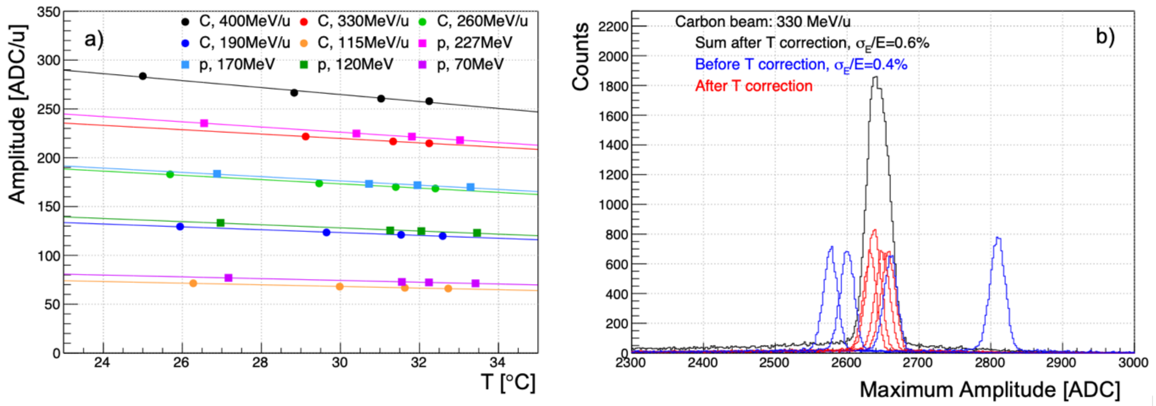

Figure 8. (a) Average values of the Maximum Amplitude (A_{MAX})/nucleon (*ADC/u*) as a function of the temperature: 4 runs, at different temperatures, were recorded at each of the 9 energies of a scan. (b) Raw measured amplitude for the 4 runs with C beams at 330 MeV/u before (blue) and after (red) the temperature correction (red), and sum of all runs after the correction (black): the energy resolution for a single run is about 0.4%, compared to 0.6% for the sum of the runs after the temperature correction.

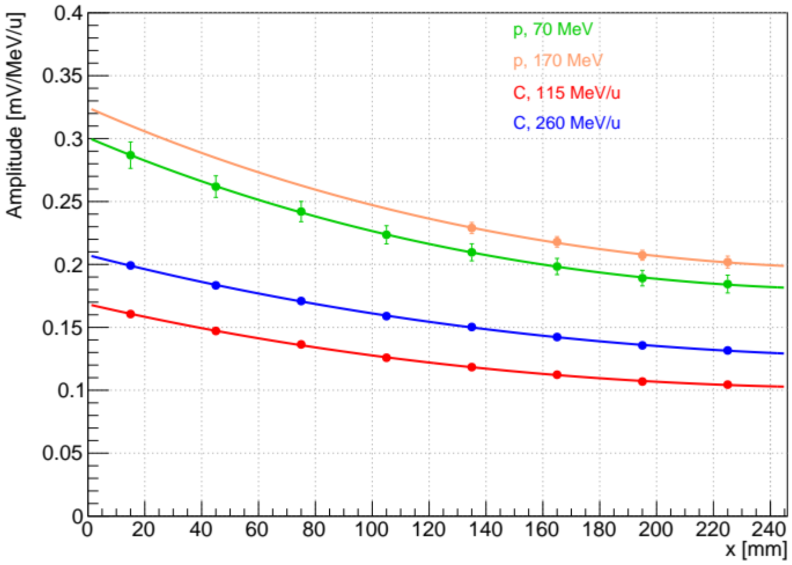

Figure 9. Maximum Amplitude as a function of the distance from the front side of the BGO crystal, for 70 MeV (green) and 170 MeV (yellow) protons, 115 MeV/u (red) and 260 MeV/u (blue) carbon ions. The lines represent the exponential fit to the data, according to eq. (2.1). The fit evaluates the attenuation coefficient (α) and the fraction of optical photons (R) that travel directly towards the photo-detector. For 170 MeV protons, when $x < 120$ mm the range is longer than the width of the 2 crystals, therefore only part of the beam energy is released in the crystals.

Figure 8(b) shows the pulse amplitude distributions obtained for 330 MeV/u carbon ions at four different temperatures, before (blue) and after (red) the correction, which is extremely effective. The comparison between the energy resolution at a fixed temperature and by combining data taken at different temperatures and corrected with the above-discussed method shows that the requirements on the energy resolution are successfully met. The energy resolution, evaluated with a gaussian fit, deteriorates from 0.4% for the data taken at different temperatures separately (blue peaks) to about 0.6% for the total sample after the correction (red peak). Taking into account that the temperature range for which we applied the temperature correction is about 10°C, while the temperature variation during a complete energy scan data acquisition was measured to be about 2°C, we concluded that the installation of the calorimeter in a temperature-controlled volume is not required, as long as the SiPM temperature is regularly monitored and their response is corrected for temperature variations.

Having validated the temperature compensation method, all the data presented in the following are temperature-corrected, with a reference value of $T = 25.3$°C.

3.4 Calibration and range correction

The experimental data acquired by firing the beam on the lateral side of the crystal at different positions show, as expected [15], that the amount of collected light, expressed in terms of Maximum Amplitude (MA), decreases exponentially as the distance between the beam position and the photodetector decreases (figure 9), according to:

$$\mathrm{MA}(x) = A[Re^{-\alpha(L-x)} + (1-R)e^{-\alpha(L+x)}] \tag{3.1}$$

where A is a normalization factor, α is the attenuation coefficient, L is the crystal length, x is the distance from the front side of the crystal, R is the fraction of the optical photons that travel directly to the SiPM tile and the remaining $(1 - R)$ fraction reaches it after having been reflected on the front side. The fit results are summarized in table 4.

Figure 9 shows the MA values as a function of the distance of the beam impinging point from the front side of the crystal, for 70 and 170 MeV protons and 115 and 260 MeV/u carbon ions. For 170 MeV protons, when $x < 120$ mm, the range is longer than the total thickness of the 2 crystals, therefore the energy measurement is not meaningful.

The beam spot size, which is about 12 mm FWHM for 70 MeV protons and 115 MeV/u carbon ions and slightly smaller for higher energies, affects the width of the amplitude distributions, but not the average values reported in the following.

Table 4. Results of the exponential fit (eq. (3.1)) on CNAO data for the Maximum Amplitude analysis. The errors on the p170 dataset are larger because only 4 beam positions are available.

Beam	Maximum Amplitude	
	α (m^{-1})	R(%)
p70	4.0 ± 0.8	9.9 ± 1.4
p170	3.8 ± 2.6	10 ± 4
C115	3.9 ± 0.2	10.2 ± 0.4
C260	3.5 ± 0.2	10.3 ± 0.4

The ratio of the observed Light Collection at depth $x = d$ (crystal length) to the one at $x = 15$ mm as a function of the distance from the front side of the crystal within the errors, is independent of the particle and the energy, consistent with the expectation that optical photon losses be independent of the origin of optical photons.

3.5 Linearity

Although, as discussed in section 2, no significant saturation effect is expected in the SiPM tile with 15 µm microcell pitch (about 1% optical pileup in a worst case scenario with 400 MeV/u ^{16}O beams), we observed the raw response is not fully linear with the incoming particle energy (figure 10(a)), for both proton and carbon beams. This is expected from light-emission mechanisms in scintillators [16]. However, having measured a dependence of the response with the emission depth of optical photons, the effect must be corrected for. In order to do so, the expected range for protons and carbon ions was simulated with FLUKA, as well as the Average Emission Depth (*AED*) of optical photons (figure 10(b)). The average emission depth provides the correction factor to be applied to raw data: indeed, we can compute the scaling factor required for the correction by dividing the expected signal at $d = 0$ and at $d = AED$.

3.6 Energy resolution

For each of the beam energies, the amplitude distribution of detected particles was analysed (figure 11): the peak corresponding to the release in the BGO crystal of the full beam energy is the dominant contribution, while a low energy tail at lower energies includes events originated by charge exchange

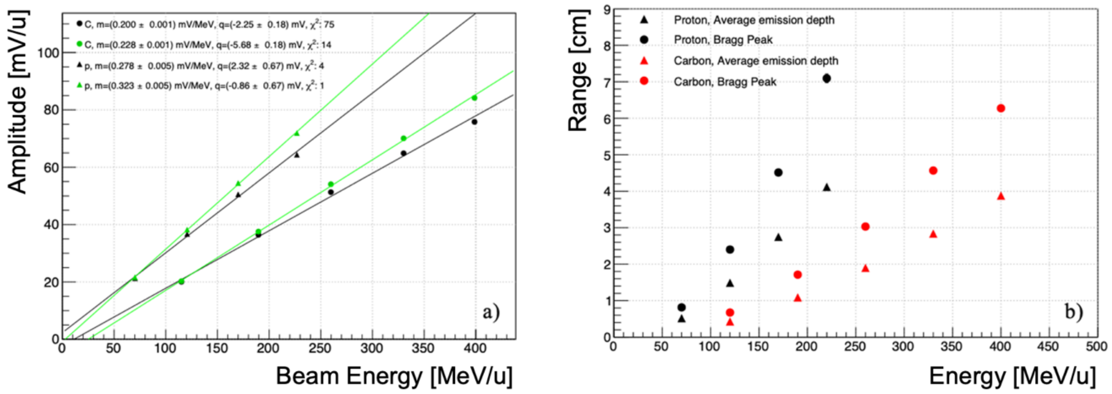

Figure 10. (a) Linearity: raw (black) and corrected (green) average values of the Maximum Amplitude (A_{MAX}) for proton and carbon ions as a function of the beam energy/nucleon. The error bars are smaller than the marker size. The correction is of the order of (11 ± 1)% and (7 ± 1)% for protons and carbon ions, respectively. (b) FLUKA simulation of the particle range and the average emission depth of optical photons in BGO, for protons and carbon ions as a function of their energy. The error bars are smaller than the marker size. Since the optical photon emission takes place all along the trajectory, the average emission depth was selected to evaluate the depth-related correction.

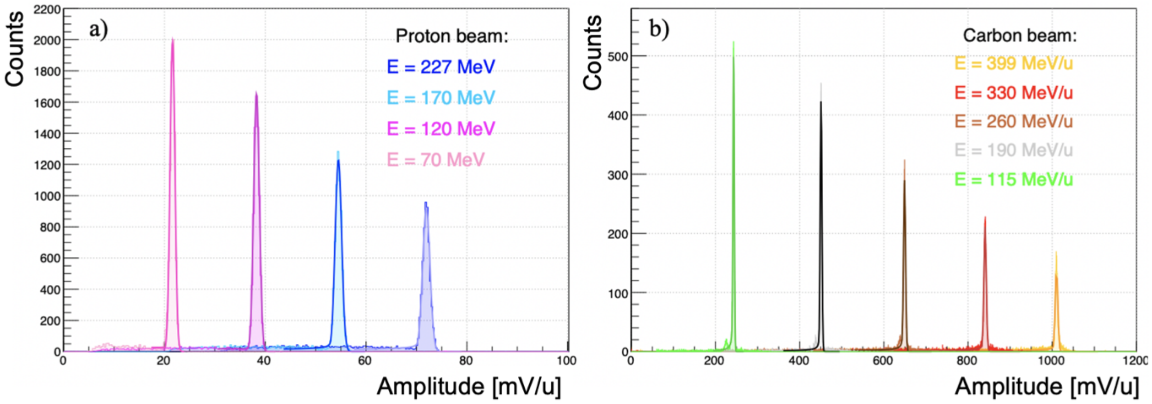

Figure 11. Maximum Amplitude (A_{MAX}) spectra for protons (a) and carbon ions (b) at different energies. The contribution of the tail corresponding to events with some missing energy increases, as expected, with the beam energy: it is related to both the beam size and the effects that cause an energy leak (e.g., target fragmentation with neutron production and, above threshold, pion production). When these correction factors are applied to raw data, the corrected data are consistent with a close to linear response (aside from quenching effects) over the explored energy range, with an angular coefficient of the linear fit that depends on the particle (figure 10(a)). The residual deviations from linearity, relevant only for the lowest energy of carbon ions, are related to the Birks effect [16].

reactions, with a neutron carrying away part of the kinetic energy, and — above threshold — by pion production. The fit with a *Crystal Ball* function [17]:

$$f(E,\alpha,n,\overline{E},\sigma) = N \begin{cases} exp\left(-\left(E-\overline{E}\right)^2/2\sigma^2\right) & \text{if } \left(E-\overline{E}\right)/\sigma > -\alpha \\ A\left(B-(E-\overline{E})/\sigma\right)^{-n} & \text{if } \left(E-\overline{E}\right)/\sigma \le -\alpha \end{cases} \tag{3.2}$$

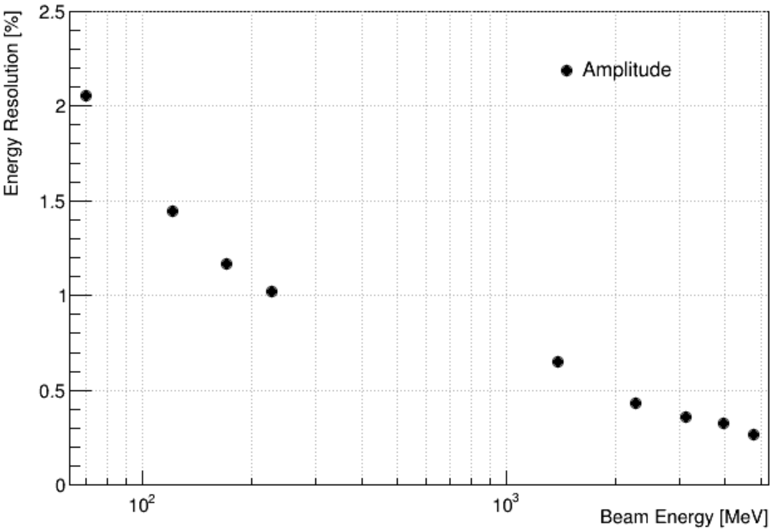

Figure 12. Energy resolution (ratio of the standard deviation of peaks in figure 11 from the fit with the *Crystal Ball* function of eq. (3.2) to the peak value) as a function of the total beam energy, from the Maximum Amplitude measurement for BGO crystals wrapped with Tyvek. The *4 (5)* points to the left (right) correspond to proton and carbon ion beams, respectively. The error bars are smaller than the marker size.

with

$$A = \left(\frac{n}{|\alpha|}\right)^n \exp\left(-|\alpha|^2/2\right)$$

and

$$B = \frac{n}{|\alpha|} - |\alpha|$$

yields the energy ($\overline{E}$) and the Gaussian σ, shown in figure 12. The energy resolution values reflect an excellent performance and are consistent with the design requirement of staying below 2% for fragments above 70 MeV.

3.7 Shape analysis

The shape of BGO signals was studied as a function of the beam particle, energy and beam position along the side of the crystal. Figure 13(a) shows the correlation between the rising time and the shape parameter (τ_r and k_s in eq (2.1), respectively) for protons and carbon ions for all the energies: the two groups are well separated, mostly thanks to the rising time parameter, shown in figure 13(b) for protons and carbon ions at all the different test energies. When the beam is fired on the long side of the BGO crystal, the rising time (figure 14) increases when the incoming point of the beam gets closer to the SiPM tile, showing that the signal shape depends on the propagation of optical photons in the crystal.

Figure 15 shows, for 70 MeV protons and 115 MeV/u carbon ions, the average value of the rising time as a function of the distance of the incoming beam from the front side. The linear fit yields a value related to the propagation speed of optical photons in the BGO. The values for protons, $v_p = (68 + -2)$ mm/ns, and carbon ions, $v_C = (64 + -1)$ mm/ns, when compared to the actual value ($v_{\text{BGO}} = c/n_{\text{BGO}} = 139$ mm/ns), provide an estimation of the average optical photon

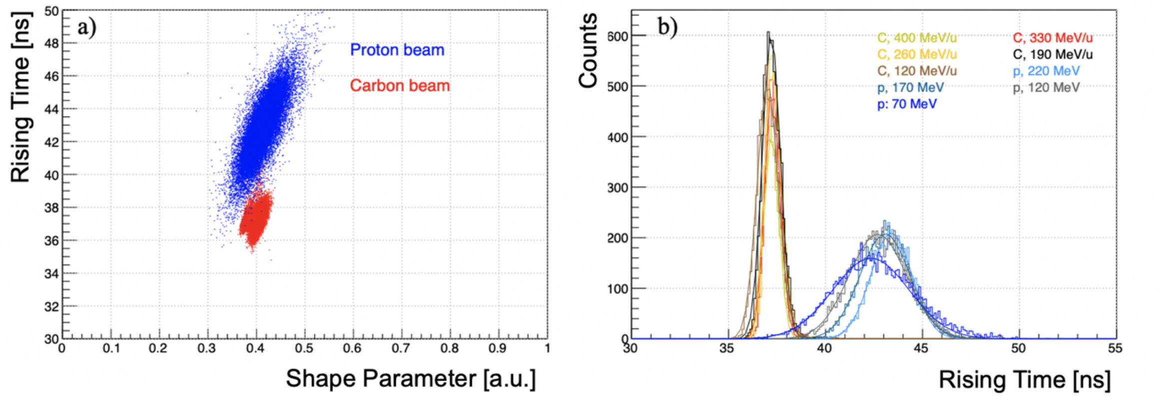

Figure 13. (a) Rising time of proton and carbon signals as a function of the shape parameter (k_s in eq. (2.1)). Data allows to separate proton and carbon ion signals with efficiency larger than 99%. (b) Rising time values for protons and carbon ions at different energies.

path length, whose ratio to the value expected for photons traveling straight to the photodetector is about $R_v = (2.11 + -0.04)$. The comparison of the rising time values obtained for protons and carbon ions also shows that the difference is independent of the beam position: therefore, the shape difference in the signal is, as expected, related to the ionisation pattern along the particle trajectory, not to a different behaviour of optical photons.

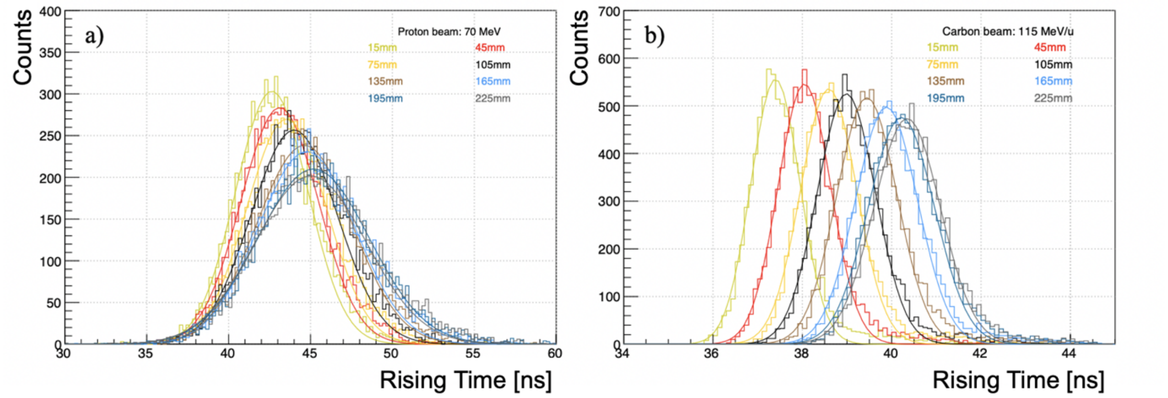

Figure 14. Rising time for 70 MeV protons (a) and 115 MeV/u carbon ions (b) as a function of the beam incoming position (distance from front face) in the BGO crystal. The rising time increases with the distance from the front face, because of the increasing difference in the travel path between photons traveling directly towards the photodetector, or away from it.

4 Discussion

The results of beam tests at CNAO were crucial in making the calorimeter design choices (crystal coating, photodetector type and configuration, readout parameters) and allowed to obtain a close to linear response with energy resolution below 2% in the full energy range foreseen by the FOOT experiment (up to at least 5 GeV).

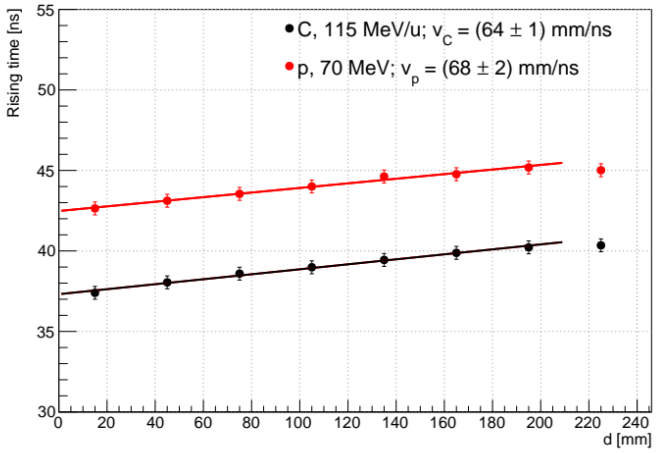

Figure 15. Average rising time for 70 MeV protons (red) and 115 MeV/u carbon ions (black) as a function of the beam incoming position (distance from front face) in the BGO crystal. The error bars represent the uncertainty on the average rising time. The last point was not included in the fit, as it is close enough to the detector (1.5 cm) that the optical photons spread asymmetrically with respect to the detector centre.

Tyvek wrapping is more efficient than mylar and reflective paint in collecting optical photons, and therefore optimizes the energy resolution. The SiPMs response did not show any deviation from linearity related to the pileup of optical photons, as long as the microcell pitch was not larger than 20 µm. The front-end board, specifically developed, sums the signals from the whole SiPM tile, and is read out by the WaveDAQ digitizer, with frequencies from 1 GS/s (used for all the tests) to 5 GS/s.

A method, based on raw data, for compensating temperature variations that cause changes in the SiPM response with a rate of about −1.4%/°C was successfully developed: a minimal deterioration of the energy resolution (0.4% to 0.6%) was observed over a range of about 10°C, much larger than expected in future FOOT data acquisition sessions.

We observed (figure 9) that the maximum amplitude of the signal decreases with the distance from the crystal front-face. To compensate for this effect, we proposed a method based on the knowledge of the range of fragments at a given energy, and the resulting response function was closer to linearity (figure 15).

The signal shape analysis allows the identification of protons and carbon ions, but it is not yet clear whether it will provide information precise enough to disentangle fragments with a similar charge to mass ratio.

The R&D stage for the FOOT calorimeter development is now completed; it provided all the information required to make the design choices required for the calorimeter construction, which was recently completed.

Acknowledgments

It is our pleasure to acknowledge the contributions by M. Mignone in the design of the front-end board and G. Alfarone and G. Scalise in the implementation of the mechanical design and the construction of the prototype. This work was partially supported by *Fondi Ricerca Locale ex 60%* from the University of Piemonte Orientale (Italy).

References

[1] M. Jermann, *Particle Therapy Statistics in 2014*, *Int. J. Part. Ther.* **2** (2015) 50.

[2] M. Durante and J.S. Loeffler, *Charged particles in radiation oncology*, *Nat. Rev. Clin. Oncol.* **7** (2009) 37.

[3] F. Tommasino and M. Durante, *Proton Radiobiology*, *Cancers* **7** (2015) 353.

[4] M. Durante and F.A. Cucinotta, *Physical basis of radiation protection in space travel*, *Rev. Mod. Phys.* **83** (2011) 1245.

[5] M. Durante, *Space radiation protection: Destination Mars*, *Life Sci. Space Res.* **1** (2014) 2.

[6] FOOT, collaborations, *Measuring the Impact of Nuclear Interaction in Particle Therapy and in Radio Protection in Space: the FOOT Experiment*, *Front. Phys.* **8** (2021) 568242.

[7] A. Ferrari, P.R. Sala, A. Fasso and J. Ranft, *FLUKA: A multi-particle transport code (Program version 2005)*, CERN-2005-010 (2005) [`DOI:10.2172/877507`].

[8] T.T. Böhlen et al., *The FLUKA Code: Developments and Challenges for High Energy and Medical Applications*, *Nucl. Data Sheets* **120** (2014) 211.

[9] R. Pleskac et al., *The FIRST experiment at GSI*, *Nucl. Instrum. Meth. A* **678** (2012) 130.

[10] L. Galli et al., *WaveDAQ: An highly integrated trigger and data acquisition system*, *Nucl. Instrum. Meth. A* **936** (2019) 399.

[11] L.F. Miller et al., *Digital pulse shape discrimination*, *Radiat. Prot. Dosimetry* **126** (2007) 253.

[12] L3 collaboration, *The Construction of the L3 Experiment*, *Nucl. Instrum. Meth. A* **289** (1990) 35.

[13] L. Scavarda, *Design and development of the Calorimeter for the FOOT experiment*, Ph.D. thesis, Università degli Studi di Torino, Torino, Italy (2022).

[14] P. Wang, Y. Zhang, Z. Xu and X. Wang, *Study on the temperature dependence of BGO light yield*, *Sci. China Phys. Mech. Astron.* **57** (2014) 1898 [`arXiv:1309.7646`].

[15] E. Auffray et al., *Crystal conditioning for high-energy physics detectors*, *Nucl. Instrum. Meth. A* **486** (2002) 22.

[16] J.B. Birks, *Scintillations from Organic Crystals: Specific Fluorescence and Relative Response to Different Radiations*, *Proc. Phys. Soc. A* **64** (1951) 874.

[17] M. Oreglia, *A Study of the Reactions* $\psi' \to \gamma\gamma\psi$, Ph.D. thesis, Stanford University, Stanford, CA, U.S.A. (1980).

The FOOT collaboration

N. Bartosik[1], F. Cavanna[1], L. Ramello[1,2], L. Scavarda[3], A. Alexandrov[4], B. Alpat[5], G. Ambrosi[5], S. Argirò[6,1], M. Barbanera[5], G. Battistoni[7], M.G. Bisogni[8,9], V. Boccia[10,4], E. Ciarrocchi[8,9], A. De Gregorio[11,12], G. De Lellis[10,4], A. Di Crescenzo[10,4], B. Di Ruzza[13], M. Dondi[14,15], M. Donetti[16], Y. Dong[7], M. Durante[10,17], R. Faccini[11,12], V. Ferrero[6,1], E. Fiorina[1], C. Finck[18], M. Francesconi[4], M. Franchini[14,15], G. Franciosini[19,12], G. Galati[20,21], L. Galli[9], G. Giraudo[1], M. Ionica[5], A. Iuliano[4], K. Kanxheri[22,5], A.C. Kraan[9], C. La Tessa[23,24], A. Lauria[10,4], E. Lopez Torres[25,1], M. Magi[19,12], A. Manna[15,14], M. Marafini[26,12], M. Massa[9], C. Massimi[14,15], I. Mattei[7], A. Mengarelli[15], A. Mereghetti[16], T. Minniti[27,28], A. Moggi[9], M.C. Montesi[4,29], M.C. Morone[27,28], M. Morrocchi[8,9], S. Muraro[7], N. Pastrone[1], V. Patera[19,12], F. Peverini[5,22], F. Pennazio[1], C. Pisanti[14,15], P. Placidi[5,30], M. Pullia[16], C. Reidel[17], R. Ridolfi[15,14], L. Sabatini[31], L. Salvi[5,22], C. Sanelli[31], A. Sarti[19,12], O. Sato[32], S. Savazzi[16], A. Schiavi[19,12], C. Schuy[17], E. Scifoni[24], L. Servoli[5], G. Silvestre[5], M. Sitta[1,33], B. Spadavecchia[6,1], R. Spighi[15], E. Spiriti[31], V. Tioukov[4], S. Tomassini[31], F. Tommasino[34,24], M. Toppi[19,12], A. Trigilio[31], G. Traini[12], G. Ubaldi[14,15], A. Valetti[6,1], M. Vanstalle[18], M. Villa[14,15], U. Weber[17], R. Zarrella[14,15], A. Zoccoli[14,15], P. Cerello[1,*]

[1] *INFN Section of Torino, Torino, Italy*
[2] *Department for Sustainable Development and Ecological Transition, University of Piemonte Orientale, Vercelli, Italy*
[3] *ALTEC, Aerospace Logistic Technology Engineering Company, Torino, Italy*
[4] *INFN Section of Napoli, Napoli, Italy*
[5] *INFN Section of Perugia, Perugia, Italy*
[6] *Department of Physics, University of Torino, Torino, Italy*
[7] *INFN Section of Milano, Milano, Italy*
[8] *Department of Physics, University of Pisa, Pisa, Italy*
[9] *INFN Section of Pisa, Pisa, Italy*
[10] *Department of Physics* E. Pancini, *University of Napoli, Napoli, Italy*
[11] *Department of Physics, University of Rome La Sapienza, Rome, Italy*
[12] *INFN Section of Roma 1, Rome, Italy*
[13] *University of Foggia, Foggia, Italy*
[14] *Department of Physics and Astronomy, University of Bologna, Bologna, Italy*
[15] *INFN Section of Bologna, Bologna, Italy*
[16] *CNAO National Center for Oncological Hadrontherapy, Pavia, Italy*
[17] *Biophysics Department, GSI Helmholtzzentrum für Schwerionenforschung, Darmstadt, Germany*
[18] *Université de Strasbourg, CNRS, IPHC UMR 7871, Strasbourg, France*
[19] *Department of Scienze di Base e Applicate per l'Ingegneria (SBAI), University of Rome La Sapienza, Rome, Italy*
[20] *Department of Physics, University of Bari, Bari, Italy*
[21] *INFN Section of Bari, Bari, Italy*
[22] *Department of Physics and Geology, University of Perugia, Perugia, Italy*
[23] *Radiation Oncology, University of Miami, Miami, FL, U.S.A.*
[24] *Trento Institute for Fundamental Physics and Applications, Istituto Nazionale di Fisica Nucleare (TIFPA-INFN), Trento, Italy*
[25] *CEADEN, Centro de Aplicaciones Tecnologicas y Desarrollo Nuclear, Havana, Cuba*
[26] *Museo Storico della Fisica e Centro Studi e Ricerche Enrico Fermi, Rome, Italy*
[27] *Department of Physics, University of Rome Tor Vergata, Rome, Italy*
[28] *INFN Section of Roma Tor Vergata, Rome, Italy*
[29] *Department of Chemistry, University of Napoli, Napoli, Italy*
[30] *University of Perugia, Perugia, Italy*
[31] *Department of Engineering, INFN Laboratori Nazionali di Frascati, Frascati, Italy*
[32] *Department of Physics, Nagoya University, Nagoya, Japan*
[33] *Department of Science and Technological Innovation, University of Piemonte Orientale, Alessandria, Italy*
[34] *Department of Physics, University of Trento, Trento, Italy*

[*] *Corresponding author*